RSC
Applied Interfaces

PAPER

View Article Online
View Journal | View Issue

Check for updates

Cite this: *RSC Appl. Interfaces*, 2024, **1**, 1285

Polymeric grating prism-based dual-mode miniature surface plasmon resonance sensor chip†

Wisansaya Jaikeandee,[a] Supeera Nootchanat,[b] Chutiparn Lertvachirapaiboon, [c] Sanong Ekgasit,[b] Kazunari Shinbo,[a] Keizo Kato[a] and Akira Baba *[a]

Received 28th June 2024,
Accepted 25th July 2024

DOI: 10.1039/d4lf00236a

rsc.li/RSCApplInter

In this study, we demonstrate the fabrication of a dual-mode miniature surface plasmon resonance (SPR) sensor using a polymeric grating prism made from a UV-curable adhesive, specifically Norland Optical Adhesive 61 (NOA 61), employing a confined sessile drop technique. The SPR excitation of the dual-mode SPR sensor chip was observed through wavelength modulation at incident angles ranging from 45° to 75° in air. The results demonstrated SPR reflectivity curves spanning the vis-NIR region. The mode of each SPR reflectivity curve was elucidated by comparing the SPR dip of the experimental results with the calculated surface plasmon (SP) dispersions. Two types of SPR modes were identified: prism-coupling SPR mode (PC-SPR mode, corresponding to $+\mathrm{SP}^0$ of the gold–NOA 61 interface) and grating-coupling SPR mode (GC-SPR mode, corresponding to $-\mathrm{SP}^{+1}$ of the gold–air and gold–NOA 61 interfaces). In deionized water ($n \sim 1.33300$), PC-SPR and GC-SPR modes at the gold–air interface were observed using a larger incident angle, whereas only the GC-SPR mode of the gold–NOA 61 interface was obtained at all incident angles. Additionally, the dual-mode SPR property was studied using different concentrations of ethylene glycol in aqueous solution ($n \sim 1.33300$–1.38313). The refractive index sensitivity obtained for the PC-SPR and GC-SPR modes at the gold–air interface was 1853 and 489.6 nm per RIU, respectively. Furthermore, the dual-mode SPR sensor demonstrated selective sensitivity by incorporating materials onto a gold-coated grating prism that matched the refractive index of the target analyte and exhibited overlapping absorption at the specific SPR excitation wavelength. Its enhanced response and significant wavelength amplification allow accurate performance in selective sensing situations. These findings underscore the dual-mode SPR sensor's potential as a powerful tool for future advanced sensing and detection applications.

1. Introduction

The surface plasmon resonance (SPR) technique is a powerful and versatile method extensively utilized for detecting refractive index changes on the sensor surface. This technique has several advantages, including label-free detection of biomolecular interactions, real-time monitoring, high sensitivity to surface changes, specificity in identifying target analytes, and nondestructiveness. These advantages have resulted in the widespread development of SPR-based sensors and biosensors for various applications such as food detection sensing, medical diagnosis, pharmaceutical development, and environmental protection.[1–6] SPR-based biosensors can be configured in various ways to accommodate different experimental requirements, encompassing prism-coupled SPR (PC-SPR), grating-coupled SPR (GC-SPR), fiber-optic SPR (FO-SPR), waveguide-coupled SPR (WC-SPR), and others.[7–9] The prism-coupling SPR system (PC-SPR), also known as the Kretschmann configuration, employs a high-refractive-index prism to couple incident light at the metal–dielectric interface, inducing SPR excitation.[10] This configuration's popularity continues growing owing to its simplicity, controllability, and potential for high electromagnetic field enhancement. However, the bulkiness of its components and the associated high operational costs constrain the integration of PC-SPR with other devices or configurations. In contrast, GC-SPR utilizes a diffraction grating, rather than a prism, to couple light at the metal–dielectric interface. The notable advantages of GC-SPR,

---

[a] Graduate School of Science and Technology and Faculty of Engineering, Niigata University, 8050 Ikarashi 2-Nocho, Nishi-ku, Niigata 950-2181, Japan. E-mail: ababa@eng.niigata-u.ac.jp
[b] Sensor Research Unit (SRU), Department of Chemistry, Faculty of Science, Chulalongkorn University, Bangkok 10330, Thailand
[c] National Nanotechnology Center (NANOTEC), National Science and Technology Development Agency (NSTDA), Pathumthani 12120, Thailand

† Electronic supplementary information (ESI) available. See DOI: https://doi.org/10.1039/d4lf00236a

including easy fabrication and cost-effectiveness, make it an attractive alternative for designing portable devices. Its adaptability for integration with other techniques enhances the overall efficiency and performance of the device.[11–16]

The combination between GC-SPR and PC-SPR have been studied through simulations[17–21] and experiments.[20,22] Introducing a grating structure with a prism can enhance SPR sensitivity and the electromagnetic field near the metal–dielectric interface. The grating structure facilitates light coupling with the surface plasmon, ensuring momentum matching similar to grating couplers in waveguides. Furthermore, the grating structure interferes with surface plasmon propagation, providing greater influence and control over the surface plasmon behaviour.[17] Simulation studies have shown that integrating the grating structure with the prism improves sensitivity,[17,19,21] produces sharper SPR resonances,[20,21] and increases the potential for selective sensing in the visible and NIR regions.[18,19] However, incorporating a nanograting on top of the prism, as observed in experimental setups, remains relatively unexplored. Most studies in this area have focused on simulation-based analyses rather than experimental investigations. In a recent study, we explored integrating a metal grating structure on a prism by fabricating a metal grating coated on a 3D-printed prism to induce SPR excitation at different wavelengths.[22] Our fabricated metal grating-coated prism demonstrated dual modes of SPR excitation simultaneously, namely PC-SPR and GC-SPR modes. Additionally, selective sensitivity allowed to controllably shift resonant dips in the SPR spectrum by employing materials with absorption wavelengths corresponding to specific SPR wavelengths.

Recently, there has been a notable advancement in developing portable microfluidic SPR sensors, reported as lab-on-a-chip systems and point-of-care diagnostics, rendering them more accessible and versatile across various applications.[2,5,23,24] An effective approach to reducing the size and cost of fabricated SPR sensors involves employing a polymeric prism instead of an expensive high-refractive-index glass prism, offering a more economical and compact solution without compromising performance. Recently, our group demonstrated the fabrication of a polymeric prism for a miniature, cost-effective SPR sensor.[25] Polymeric lenses, with diameters ranging from 2.5 to 6.0 mm, were fabricated using the confined sessile drop technique to serve as a prism component in the SPR sensor. This technique allows the creation of disposable miniature SPR sensor chips. The polymeric lens used as the SPR prism was fabricated using Norland Optical Adhesive 61 (NOA 61), an optical polymer known for its favourable properties. NOA 61 has a high refractive index (RI) of approximately 1.56, facilitating efficient light coupling into the SPR sensor.[25,26] Additionally, NOA 61 exhibits low shrinkage and rigidity, ensuring the long-term stability and reliability of the polymeric lens within the SPR device. Combining a polymeric prism and NOA 61 as the lens material is a promising approach for developing SPR devices. The advantages of NOA 61, including its high RI, low shrinkage, and rigidity, render it suitable for prism design and enable efficient light transmission. This innovative approach to device fabrication contributes significantly to the ongoing development and improvement of SPR-based biosensing technologies, paving the way for further enhancements in device performance and expanded applications.

In this study, we investigated the NOA 61 polymeric grating prism, notable for its seamless interface achieved through the confined sessile drop technique, ensuring a smooth and uninterrupted connection between the grating structure and the prism itself. This prism configuration's key feature is its seamless integration, providing various advantages, particularly in SPR and biosensing applications. Integrating the grating pattern on the prism surface introduces additional plasmon resonances that couple with incident light, enabling SPR excitation at NIR wavelengths. This integration extends the SPR sensing range, enhances sensitivity, and improves detection accuracy in the NIR region. By leveraging the advantages of PC-SPR and GC-SPR, we achieve a comprehensive and extended sensitivity profile across a broader spectral range.

2. Experimental methods

2.1 Materials and chemical reagents

Norland Optical Adhesive 61 (NOA 61) was purchased from Norland Products Inc. The Sylgard 184 silicone elastomer kit (polydimethylsiloxane, PDMS) was obtained from Dow Corning Toray Corporation. Ethylene glycol (EG), ethanol 95% v/v, and 2-propanol were purchased from Kanto Chemical Co., Inc. Nitric acid (HNO_3), 11-mercaptoundecanoic acid (11-MUA), phosphate-buffered saline (PBS, pH 7.4), monoclonal antihuman IgG (Fab specific) antibody produced in goat, IgG from human serum, *N*-hydroxysuccinimide (NHS), 1-ethyl-3-(3-dimethylaminopropyl)-carbodiimide hydrochloride (EDC), ethanolamine hydrochloride (EA-HCl), 1,3-propanedithiol (PDT), sodium 3-mercapto-1-propane-sulfonate (MPS), poly(diallyldimethylammonium chloride) solution (PDADMAC, M_w = ∼200 000–350 000), and poly(sodium 4-styrenesulfonate) (PSS, M_w = 70 000) were purchased from Sigma-Aldrich. A carboxyl gold nanorod (25 nm diameter) in aqueous solution (carboxyl-PEG5000-SH) with a maximum absorption wavelength spectra at 650 nm was purchased from Cytodiagnostics Inc. A gold nanorod (9 nm × 45 nm size) in aqueous solution with a maximum absorption wavelength of 900 nm was obtained from Dai Nippon Tokyo Co., Ltd. All solutions were prepared using deionized (DI) water without additional purification. A polycarbonate recordable Blu-ray disc (BD-R, grating pitch = 320 nm) was obtained from Taiyo Yuden Co., Ltd.

2.2 Fabrication of the dual-mode SPR sensor chip

The fabrication process of the dual-mode SPR sensor chip is shown in Fig. S1 (A–C) in the ESI† with the three processes classified as follows: (A) the preparation of a grating-PDMS circular disk by soft lithography, (B) the fabrication of the NOA 61 polymeric grating prism using the confined sessile drop technique, and (C) the formation of the Au film on the fabricated prism. To prepare the grating-PDMS circular disk, the BD-R master template was first cut into small 2.5 × 2.5 cm^2 pieces. These BD-R template pieces underwent a cleaning process to remove the organic dye, involving immersion in a 60–61% v/v HNO_3 for 15 min, followed by sonication in detergent water, tap water, and twice in deionized (DI) water for 15 min each. The cleaned BD-R template was then dried using an N_2 stream. Next, the PDMS precursor, prepared by mixing PDMS base and curing agent at a 10 : 1 w/w ratio, was cast onto the cleaned BD-R templates. After eliminating air bubbles in a vacuum chamber, the PDMS precursor was cured at 60 °C for 3.5 h to imprint the negative grating pattern on the PDMS substrate. A 6.0 mm diameter grating-PDMS circular disk was obtained by punching the cured PDMS substrate with a hollow puncher. Subsequently, the grating-PDMS circular disk was affixed to a glass slide, with the grating side facing upward. Liquid NOA 61 was dropped directly onto the grating-PDMS circular disk. Liquid NOA 61 spreads until reaching the edge of the PDMS circular disk and formed a hemispherical shape. The shape of the resulting prism can be controlled by adjusting the amount of liquid NOA 61. Using insufficient and excessive amounts of liquid NOA 61 cannot form a prism owing to the limitations imposed by the substrate. Gibb's inequality equation provides a theoretical framework for understanding this limitation.[27,28] The hemispherical prism was left at room temperature for 30 min to stabilize, ensuring the grating's structural integrity. Afterward, the NOA 61 polymeric grating prism was obtained by curing the hemispherical prism under UV irradiation (λ = 350–380 nm) on both sides for 1 h. The NOA 61 polymeric grating prism was fabricated on a grating-PDMS substrate instead of directly on the BD-R template due to several factors. First, the strong adhesion of NOA 61 to the BD-R template complicates removal and increases the pattern defects. In addition, PDMS, known for its flexibility, allows for effective molding and imprinting, ensuring accurate grating pattern replication. Previous studies showed that PDMS was easily cut into circular disks, making it ideal for forming NOA 61 polymeric prisms.[25] This approach enhances the quality and repeatability of the fabrication process. The NOA 61 polymeric prism was formed using the confined sessile drop technique because this technique provides a precise control over droplet shape and size, leading to highly reproducible prism geometries crucial for maintaining optical stability.[28] Geometric deformation can affect SPR response,[25] so the study focused on fabricating prisms of one size to avoid deformation factor and ensure sensor performance. In the final step, the grating side of the fabricated prism was subjected to thermal evaporation, depositing a 3 nm Cr film and a 47 nm Au film. The Cr layer is essential for strong adhesion of the Au layer to the prism. This Cr and Au thickness condition wase chosen because we use PC-SPR and GC-SPR at the Au/air (or aqueous solution) interface, which are coupled with evanescent wave in total reflection condition, for the sensor application. After metal deposition, the NOA 61 polymeric grating prism reveals a distinctive line diffraction pattern, depicted in Fig. 1A. In our previous work, we created the miniature NOA 61 polymeric prism using a confined sessile drop technique, resulting in a flat base surface without any observable rainbow colours of the diffraction pattern (refer to Movie S1†). In contrast, our current study further advances the miniature NOA 61 polymeric prism using enhanced soft lithography to imprint nanostructures on the base side. This development allows the NOA 61 polymeric grating prism to exhibit clearly visible line diffraction patterns, as seen in Movie S2,† providing valuable insights into the grating structure's characteristics and behaviour.

To design a dual-mode SPR sensor chip incorporating PC-SPR and GC-SPR excitation modes, the fabricated prism was integrated with a 3D-printed microfluidic cell created using a 3D printer (Ultimaker 3, Ultimaker B.V., Netherlands). The resulting dual-mode SPR sensor chip, with an approximate size of 2.5 × 2.5 cm^2, is shown in Fig. 1B, offering visual representations of the device in front and side views. Fig. 1C provides a schematic depicting the SPR excitation process within the sensor chip.

2.3 SPR biosensor for human IgG detection

To modify the biosensing surface for human IgG detection, the initial step involved immersing the fabricated SPR sensor

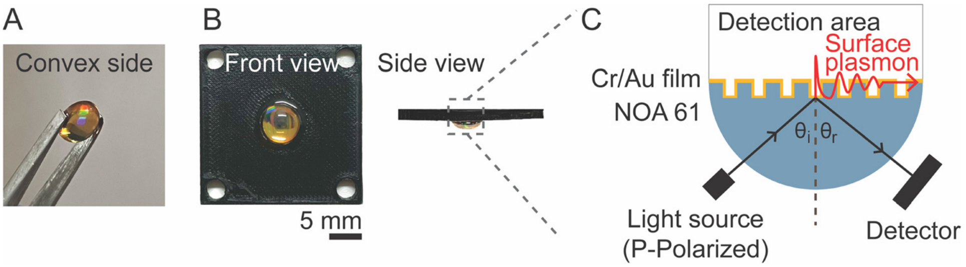

Fig. 1 (A) Grating diffraction pattern on convex side of NOA 61 polymeric grating prism (B) front and side views of the dual-mode SPR sensor chip. (C) Schematic representation of the internal microfluidic cell structure, illustrating the underlying mechanisms governing the SPR excitation process within the dual-mode SPR sensor chip.

chip in a 0.1 M 11-MUA in ethanol solution at room temperature for 2 h. Subsequently, a baseline rinse was performed using a 0.01 M PBS buffer solution. Following this, an aqueous solution containing 0.4 M EDC and 0.1 M NHS in a 1 : 1 v/v ratio was employed to activate the sensing surface for 15 min. Then, the mixture was rinsed with a PBS buffer solution. The immobilization of 100 μg mL^{-1} human IgG was performed for 30 min, after which noncovalently bound antibodies were removed using a PBS buffer solution. Next, the biosensor surface was treated with a 0.2 M EA-HCl aqueous solution for 15 min to block nonspecific binding sites, followed by a rinse with a PBS buffer solution. In the final step, 100 μg mL^{-1} human IgG was introduced for 30 min, and the sensor surface was rinsed with a PBS buffer solution. SPR sensorgrams were recorded before initiating the surface activation procedure.

2.4 Surface modification using gold nanorods (AuNRs)

The gold film-coated NOA 61 polymeric grating prism underwent a 12 h immersion in a 10 mM solution of 1,3-propane dithiol (PDT) in ethanol, where PDT served as a linking agent between the gold film and AuNRs. PDT's thiol head group (–SH) formed a strong covalent bond with the gold film, while the other end interacted with the AuNRs. Following immersion in the PDT solution, the gold film was placed in an aqueous solution containing 5 ppm of AuNRs 650 (or 20 ppm of AuNRs 900) for 6 h. This process facilitated the attachment of AuNRs to the gold film *via* the functional groups of PDT. The resulting assembly formed a hybrid structure comprising a gold film, a PDT linker, and AuNRs as one layer.

2.5 Formation of PDAMAC/PSS layer-by-layer thin films on the surface of the dual-mode SPR sensor chip

To prepare the PDADMAC/PSS bilayer, the gold film-coated NOA 61 polymeric grating prism was functionalized with MPS, introducing a negative charge. The Au surface was coated with MPS by immersion in a 1 mM MPS solution for 3 h. Subsequently, the functionalized surface was immersed in a 4% w/w PDADMAC solution (0.4 mL) for 15 min. Following this, the PSS layer was deposited onto the PDADMAC layer by immersing the surface in a 1 mg mL^{-1} PSS solution (0.4 mL), forming a bilayer structure. Throughout the process, DI water served as the solvent for all solutions, and each step was followed by rinsing with 5 mL of DI water.

2.6 Characterization

Atomic force microscopy (AFM, SPM-9600, Shimadzu Corporation) was employed to examine the surface morphology of the fabricated grating prism, offering valuable insights into its surface characteristics and uniformity. For wavelength-modulated SPR characterization, a home-built SPR setup was utilized to measure the SPR reflectivity spectrum (Fig. S2 in ESI†). White light emitted by a halogen source (HL-2000, Ocean Optics) was channelled into a 600 μm optical fiber (F600-UVVis-SR, StellarNet Inc) through a collimating lens (74-VIS, Ocean Optics). The light beam was passed through a linear polarizer, an aperture with a diameter of 0.7 mm, and a biconvex lens with a focal length of 15 cm. These components ensured precise control over the light path, directing it onto the dual-mode SPR sensor chip mounted on a θ–2θ motorized goniometer. The reflected light was collected using a plano-convex lens with a focal length of 12 mm and a 600 μm optical fiber (F600-UVVis-SR, StellarNet Inc). The collected light was then directed to a vis-NIR spectrometer (USB 4000, Ocean Optics). OP Wave software facilitated characterization and data processing. To obtain the SPR reflectivity curve, the signal reflected from the substrate under p-polarization was divided by the signal reflected from the substrate under s-polarization. This calculation allowed us to extract specific SPR reflectivity values, providing valuable insights into the surface plasmon resonance phenomenon on the substrate.

3. Results and discussion

3.1 Surface morphology

We utilized AFM for surface morphology characterization to examine the imprinted grating pattern on the base side of the NOA 61 polymeric grating prism. The AFM image of the standard BD-R grating template revealed a uniform grating pattern with a pitch of approximately 320 nm and a height of approximately 32 nm, as shown in Fig. 2A. As outlined in the experimental section, this BD-R grating pattern was replicated onto PDMS, forming a grating-PDMS circular disk. Using the confined sessile drop technique, a grating-PDMS circular disk was used to fabricate the NOA 61 polymeric grating prism. Following UV curing, the grating-PDMS circular disk was easily detached, leaving behind the NOA 61 polymeric prism with the grating pattern on its base side, as illustrated in Fig. 2B. The resultant NOA 61 polymeric prism exhibited an imprinted pattern with a grating pitch of approximately 320 nm and a height of approximately 32 nm after the deposition of Cr–Au films, mirroring the structure of the original grating template. Using the grating-PDMS

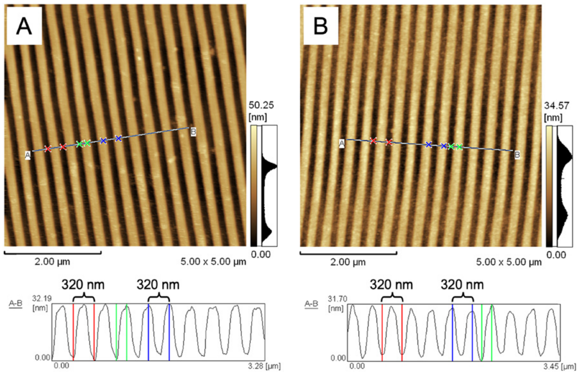

Fig. 2 AFM images (5 μm × 5 μm) showing the surface morphology of (A) the standard BD-R grating and (B) the gold-coated side of the NOA 61 polymeric grating prism.

circular disk in the confined sessile drop process, we successfully fabricated the NOA 61 polymeric prism with a grating structure, showcasing its potential application in various optical or sensing devices.

3.2 SPR characterization

The performance evaluation of the dual-mode SPR sensor chip was conducted using a wavelength-modulated SPR characterization method. The SPR reflectivity curves of the dual-mode SPR sensor chips were analyzed at incident angles ranging from 45° to 75°. At incident angles between 45° and 50°, a redshift of the SPR excitation dip was observed in the near-infrared (NIR) region within a wavelength range of 800–825 nm, as illustrated in Fig. 3A. Upon increasing the incident angle to 51°, SPR excitation dips were detected in the visible region at a wavelength of 650 nm alongside the NIR region, as shown in Fig. 3B. Further increasing the incident angle beyond 56° resulted in a redshift in the SPR excitation dips at 680 to 750 nm and 850 to 930 nm wavelengths. Conversely, a blueshift of the SPR excitation dips was observed in the wavelength range of 450–600 nm (Fig. 3C). These observations provide valuable insights into the behaviour and characteristics of the fabricated SPR sensor chips under varying incident angles. The SPR excitation occurs when the momentum of the incident light in the plane parallel to the surface matches with the momentum of the SP through using prism coupling or grating coupling for their excitation.[8,29] Considering that the optical geometry of the SPR sensor is shown in Fig. 1C, the SPR configuration consists of a three-layer system with a thin metal grating film placed between two dielectric materials with differing dielectric constants: a low dielectric constant material (dielectric medium) and a high dielectric constant material (prism). Using a diffraction grating, further coupling momentum is derived for the SP dispersion relation as the sum of the wavevector component of the incident angle. The wavevector of the incident light parallel to the surface (K_{px}) with grating wavevector (G) is written by the following equation:

$$K_{\mathrm{sp}} = K_{\mathrm{px}} + G = \frac{2\pi}{\lambda}\sqrt{\frac{\varepsilon_{\mathrm{m}}(\omega)\varepsilon_{\mathrm{d}}(\omega)}{\varepsilon_{\mathrm{m}}(\omega)+\varepsilon_{\mathrm{d}}(\omega)}}\sin\theta_{\mathrm{i}} + \frac{2\pi}{\Lambda}m \qquad (1)$$

where λ is the wavelength, $\varepsilon_{\mathrm{m}}(\omega)$ and $\varepsilon_{\mathrm{d}}(\omega)$ are the wavelength-dependent dielectric constants of gold and medium, described by the classical Drude's free electron model, m is the diffraction order, Λ is the grating pitch, K_{sp} represents the SP wavevector, and K_{px} represents the wavevector component parallel to the surface of the incident light.[30–32] To elucidate the observed SPR reflectivity curves, the dispersion relation of surface plasmons (SP) was considered to clarify the origin of the observed SPR excitation. The SP dispersion relation was calculated using the eqn (1). The SPR dips observed in the experimental results were plotted and compared with the analysis of the SP dispersion relation, as shown in Fig. 3D. As the incident angle increased from 45° to 75°, the observed SPR dips (black dots) in the 800–950 nm wavelength range were attributed to the GC-SPR mode occurring at the gold–NOA 61 polymeric grating prism interface (black line), representing the $-\mathrm{SP}^{+1}$ mode. These observed SPR excitations originated from the gold–NOA 61 polymeric grating prism interface, thus were inactive for sensing purposes. This conclusion was substantiated by an experiment involving a 100 nm gold-coated NOA 61 polymeric grating prism, where only GC-SPR at the gold layer-NOA 61 polymeric grating prism interface could be excited (Fig. S3 in the ESI†). In contrast, the

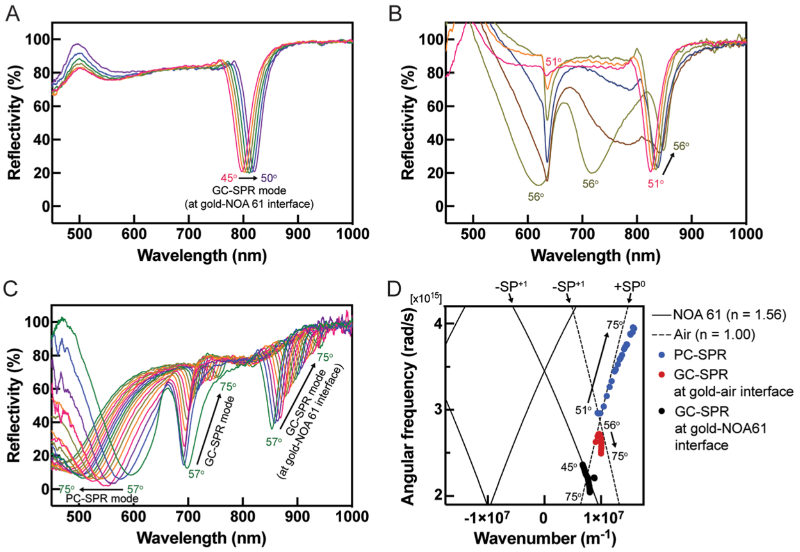

Fig. 3 SPR reflectivity curves in the air (n = 1.000028) of the dual-mode SPR sensor chip at various incident angles: (A) 45–50°, (B) 51–56°, and (C) 57–75°. (D) Experimental results of dual-mode SPR, encompassing PC-SPR mode (blue dots), GC-SPR mode at the gold–air interface (black dots), and GC-SPR mode at the gold–NOA 61 interface (red dots), and calculated results of the dispersion of SPs at the gold–NOA 61 (full lines) and gold–air (dash line) interfaces.

red dotted plots of the experimental results corresponded to the GC-SPR mode at the gold–air interface, representing the $-SP^{+1}$ mode. The red dots became observable at higher incident angles. Simultaneously, blue dotted plots corresponded to the PC-SPR mode at the gold-coated grating prism–air interface (dashed line) with $+SP^0$ mode. This PC-SPR mode was observed at an incident angle of more than 51° and a wavelength of 625 nm. Consequently, the observed SPR excitation within the specified incident angle and wavelength range can be attributed to both the PC-SPR and GC-SPR modes between the gold-coated grating prism and the surrounding medium. These findings indicate that when the fabricated SPR sensor chip is utilized at higher incident angles, it can provide PC-SPR and GC-SPR excitation modes, allowing for versatile SPR sensing capabilities.

3.3 Evaluation of reflectance dependence on the incident angle

The dependence of reflectance on the incident angle was investigated in an aqueous solution (DI water). Redshifts in the SPR reflectivity curves, evident at incident angles of 45–75° in Fig. 4A and extending to incident angles of 76–85° in Fig. 4B, at wavelengths ranging from approximately 750 to 885 nm, were attributed to the GC-SPR mode at the gold–NOA 61 interface. This indicated that the GC-SPR mode at the interface between the gold layer and NOA 61 was observable across incident angles from 45° to 85°. Moreover, blueshifts in the SPR excitations occurred in two distinct wavelength ranges: 790 to 625 nm when the incident angle exceeded 76° and 835 to 820 nm when the incident angle surpassed 81°, as illustrated in Fig. 4B. The PC-SPR mode could be observed with an incident angle greater than 76°, while the GC-SPR mode at the gold–air interface became apparent with an incident angle exceeding 81°. Fig. 4C shows plots of the SPR excitation wavelengths for different SPR modes as a function of the incident angle. The focus on an incident angle greater than 81° represents dual-mode excitations. The PC-SPR mode (blue circles) and the GC-SPR mode at the gold–air interface (red squares) exhibited a wavelength shift ($\Delta\lambda$) of approximately 97.5 and 14.25 nm, respectively, as the incident angle varied. This suggests that the PC-SPR mode provided greater sensitivity than the GC-SPR mode at the gold–air interface to variations in incident angles. The impact of changes in the incident angle on the GC-SPR mode at the gold–NOA 61 interface (black triangles) was negligible. The SP dispersion in Fig. 3D further clarifies that changes in the incident angle resulted in minimal shifts in the SPR excitation within the GC-SPR mode at the gold–NOA 61 interface. Adjustments in the incident angle led to slight changes in the SPR excitation within the GC-SPR mode at the gold–NOA 61 interface, indicating insensitivity to such changes. However, practical applications of the dual-mode SPR sensor should involve calibration to accommodate variations in the SPR reflectivity curves.

3.4 Evaluation of reflectance dependence on refractive index

The refractive index dependence of SPR reflectivity was modulated by varying the concentration of EG, acting as the dielectric medium, with each EG concentration corresponding to a distinct refractive index within the range of 1.33300 to 1.38313.[33] Experiments at a 45° incident angle with different EG refractive indices, as depicted in Fig. 5A, demonstrated that an increase in EG concentration and refractive index yielded no observable changes in the SPR excitation. This is explained that the SPR dips in this wavelength range are originated from the gold–NOA61 interface as discussed using the SP dispersion calculation in Fig. 3. From eqn (1), the SPR excitation condition depends on the dielectric constants of both ε_m and ε_d at the interface where SP is excited. At the gold–NOA61 interface, ε_d corresponds to the dielectric constant of NOA61, hence both dielectric constants, ε_m and ε_d, are constant even when the refractive index of EG was varied. This finding suggested that the GC-SPR mode at the gold–NOA 61 interface displayed insensitivity to variations in the refractive index of the surrounding medium. Conversely, at a fixed incident angle of 85°, as illustrated in Fig. 5B, redshifts in SPR excitation were observed with increasing EG concentration. Specifically, the PC-SPR and GC-SPR modes at the gold–air interface exhibited these redshifts, indicating the sensor's sensitivity to changes in the refractive index. The SPR dips of the GC-SPR mode at the gold–NOA 61 interface were obtained only at a specific wavelength of approximately 939 nm, confirming the limited operational range and insensitivity of the GC-SPR mode at the gold–NOA 61 interface to changes in the refractive index compared to the PC-SPR and GC-SPR modes at the gold–air

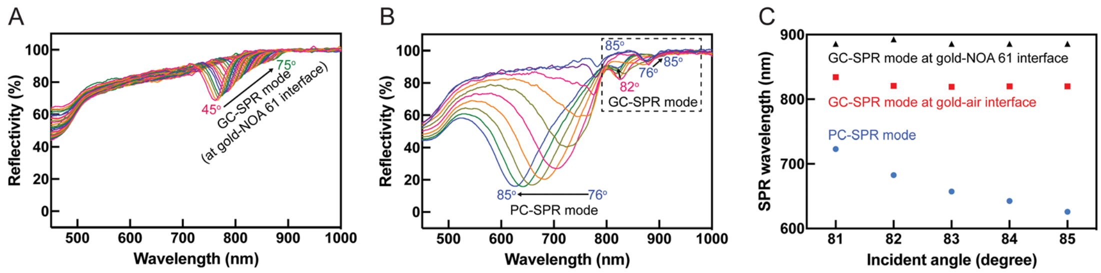

Fig. 4 SPR reflectivity curves in an aqueous solution (n = 1.33300) of the dual-mode SPR sensor chip at various incident angles: (A) 45–75° and (B) 76–85°. (C) Plots illustrating the SPR wavelength excitation of PC-SPR (blue circle), GC-SPR mode at the gold–air interface (red square), and GC-SPR mode at the gold–NOA61 interface (black triangle) as a function of the incident angle within the range of 81–85°.

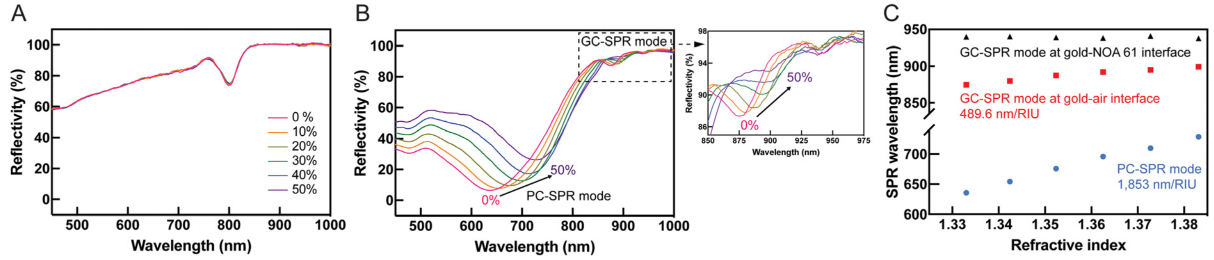

Fig. 5 SPR reflectivity curves of an ethylene glycol aqueous solution (0–50% w/w, n = 1.33300–1.38313) were observed at incident angles of (A) 45° and (B) 85°. (C) Plots illustrating the excitation wavelength for SPR in PC-SPR mode (blue circle), GC-SPR mode at the gold–air interface (red square), and GC-SPR mode at the gold–NOA61 interface (black triangle) as a function of the refractive index.

interface. Quantifying the refractive index sensitivity of the dual-mode SPR sensor (Fig. 5C) revealed that the PC-SPR mode exhibited higher sensitivity at 1853 nm per refractive index unit (RIU) compared to the GC-SPR mode at the gold–air interface, which had a sensitivity of 489.6 nm per RIU. These results highlight the superior responsiveness of the PC-SPR mode to changes in the refractive index compared to the GC-SPR mode at the gold–air interface. Additionally, the GC-SPR mode at the gold–NOA 61 interface remained unaffected by changes in the refractive index.

3.5 SPR biosensor for human IgG detection

To showcase the functionality of the dual-mode SPR sensor chip as a biosensor, a feasibility study was undertaken to detect human IgG. Fig. S4† shows the straightforward experimental protocol, commencing with using 11-MUA to modify the sensor surface and establishing a carboxylic acid (–COOH)-terminated alkane thiol layer on the gold surface. Amino-containing molecules, such as proteins, were immobilized by activating the carboxylic acid (–COOH)-terminated groups on the biosensor surface using NHS catalyzed by EDC. Following this activation step, anti-IgG at 100 μg mL^{-1} concentration was immobilized on the biosensor surface. The biosensor surface was treated with an EA-HCl aqueous solution to prevent nonspecific adsorption of the target anti-IgG. Activated anti-IgG was then used to adsorb IgG at a 100 μg mL^{-1} concentration. The sensing system exhibited a significant real-time response throughout the modification process in the PC-SPR mode (Fig. 6A) and GC-SPR mode in the gold-PBS buffer solution (Fig. 6B). The SPR response in both PC-SPR mode and GC-SPR mode at the gold-PBS buffer solution interface demonstrated a clear initial signal increase, followed by a gradual rise as anti-IgG coherently attached to the biosensor surface and human IgG adsorbed on the sensing surface. In contrast, the GC-SPR mode at the gold–NOA 61 interface exhibited no response despite biosensor surface activation, as depicted in Fig. 6C. The utilization of human IgG for observing SPR phenomena at the interface is a well-established and widely adopted method. Detectable changes on the surface were apparent in both PC-SPR and GC-SPR modes at gold-PBS solution interface. This compelling evidence prompted further investigations into the selectivity of the sensor, aiming to inquire deeper into its capability to identify and differentiate specific changes in the sensing environment.

3.6 Selectivity of the dual-mode SPR sensor

To examine the selective mode in the fabricated dual-mode SPR sensor chip, gold nanorods (AuNRs) with longitudinal localized plasmon excitation at wavelengths of 650 nm (AuNRs 650) and 900 nm (AuNRs 900) (Fig. S5 in the ESI†) were selected for functionalizing the gold surface-coated NOA

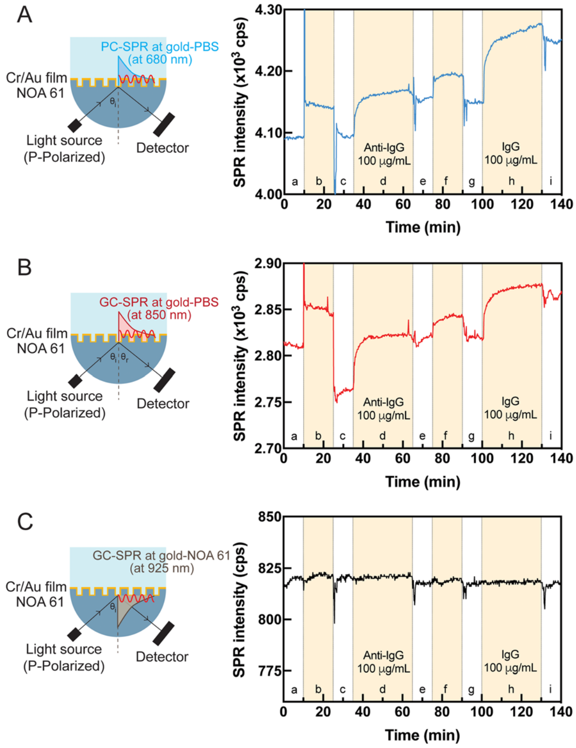

Fig. 6 Schematic drawing and real-time sensorgram at the excitation wavelength of (A) PC-SPR (blue line) and GC-SPR at (B) the gold-PBS buffer solution interface (red line) and (C) the gold–NOA 61 interface (black line). The abbreviations over the x-axis injection order for detection included a: PBS buffer solution, b: EDC/NHS, c: PBS buffer solution, d: 100 μg mL^{-1} of anti-IgG, e: PBS buffer solution, f: EA-HCl, g: PBS buffer solution, h: 100 μg mL^{-1} of IgG, and i: PBS buffer solution.

61 polymeric prisms before monitoring the formation of PDADMAC/PSS bilayers. This was done before monitoring the formation of PDADMAC/PSS bilayers because the localized plasmon excitation wavelengths of AuNRs 650 and 900 correspond to the PC-SPR and GC-SPR excitation wavelengths, respectively. The formation of PDADMAC/PSS bilayers is commonly employed to study the ability of SPR sensors owing to their facile nanoscale fabrication and versatility. The PDADMAC/PSS bilayers were assembled using the layer-by-layer deposition technique. Tunable properties were achieved by alternately depositing PDADMAC/PSS, rendering them valuable components for developing sensitive and selective SPR sensing platforms. The gold surface-coated NOA 61 polymeric prisms were integrated with AuNRs to ensure the dual-mode SPR sensor device could selectively detect modes at specific wavelengths. This integration enhanced the capability to selectively analyze and detect specific biomolecular interactions or target analytes with improved sensitivity and specificity.

To observe tunable shifts in SPR wavelengths associated with AuNRs, four layers of AuNRs, each with specific absorption peaks at 650 and 900 nm, were deposited on the gold film-coated NOA 61 polymeric prisms. This multilayer configuration allowed for precise control and manipulation of the SPR response. Multiple AuNR layers influenced the collective plasmonic behaviour, resulting in significant shifts in the SPR wavelengths, as illustrated in Fig. 7. The observed SPR reflectivity curves displayed a redshift in PC-SPR and GC-SPR modes at the gold–air interface after depositing four layers of AuNRs 650 (Fig. 7A) and 900 (Fig. 7B). The relationship between $\Delta\lambda$ and the number of AuNR layers was plotted. The addition of AuNRs 650 produced a greater wavelength shift than AuNRs 900 in the PC-SPR mode (Fig. 7C), whereas the GC-SPR mode at the gold–air interface exhibited a greater wavelength shift with the addition of AuNRs 900 (Fig. 7D). This result indicates that sensitivity can be enhanced when the absorption wavelength of the binding materials on the gold surface matches the excited SPR wavelength. Furthermore, the addition of AuNRs increased the density of gold on the surface, disrupting the uniformity of the grating pattern. The AuNRs adhered to the grating structure, filling the gaps between the grating pitches (Fig. S6 in the ESI†). Consequently, the presence of AuNRs caused the grating to lose its uniformity, affecting the SPR reflectivity. As a result, the SPR reflectivity broadened as the AuNR layer increased.

Fig. 8 presents SPR reflectivity curves of PDADMAC/PSS bilayers ranging from 2 to 8 bilayers under different experimental conditions: (A) without AuNRs, (B) with 2 layers of AuNRs 650, and (C) with 2 layers of AuNRs 900. These results illustrate that SPR dips in PC-SPR and GC-SPR at the gold–air interface under all experimental conditions exhibit a redshift with increased PDADAMAC/PSS bilayers. Furthermore, the linear regression plot between $\Delta\lambda$ and the number of bilayers, without AuNRs (black color), with 2 layers of AuNRs 650 (blue color), and with 2 layers of AuNRs 900 (red color), is depicted in Fig. 9A, focusing on the PC-SPR mode, and Fig. 9B, focusing on the GC-SPR mode at the gold–air interface. Our findings reveal that introducing two layers of AuNRs 650 significantly increased the slope of the linear fitting in the PC-SPR mode in the wavelength range from 633 nm to 673 nm compared to the absence of AuNRs, showing a 1.32-fold enhancement. It also resulted in a slightly higher slope than adding two layers of AuNRs 900, exhibiting an increase of approximately 1.05 times in comparison. In contrast, the GC-SPR mode at the gold–air interface in the wavelength range from 882 to 899 nm exhibited a significantly higher slope in the linear fitting when 2 layers of AuNRs 900 were added, compared to the

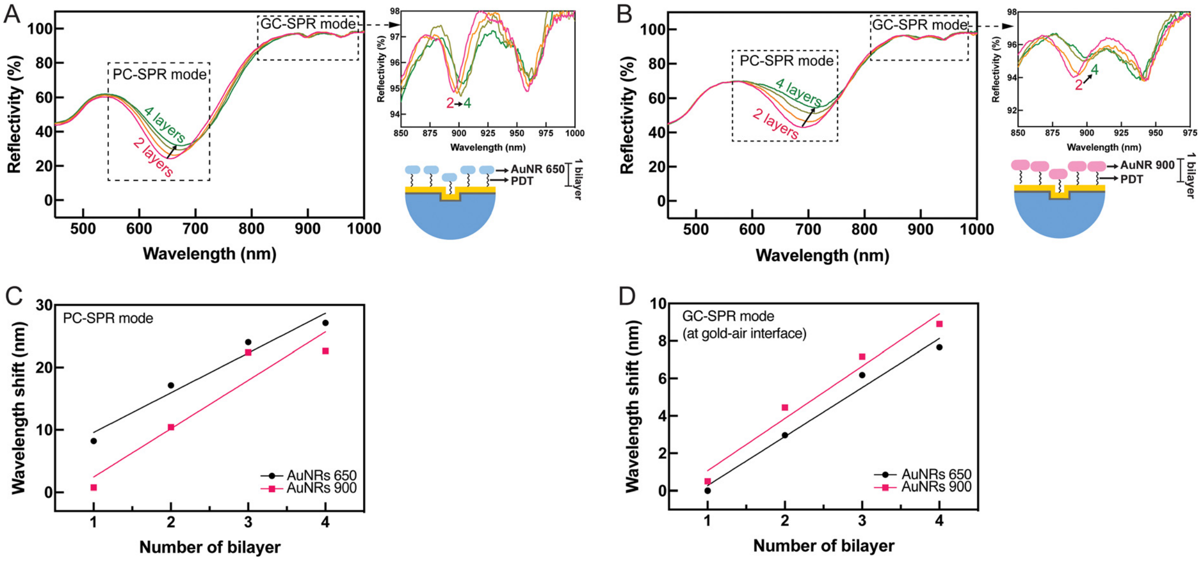

Fig. 7 Reflectivity curves for SPR, illustrating the formation of (A) AuNRs 650 and (B) AuNRs 900 on a gold-coated NOA 61 polymeric grating prism for 4 layers. Plots of wavelength shift and the number of AuNRs 650 layers (black color) and AuNRs 900 (red color) in (C) the PC-SPR mode and (D) the GC-SPR mode at the gold–air interface.

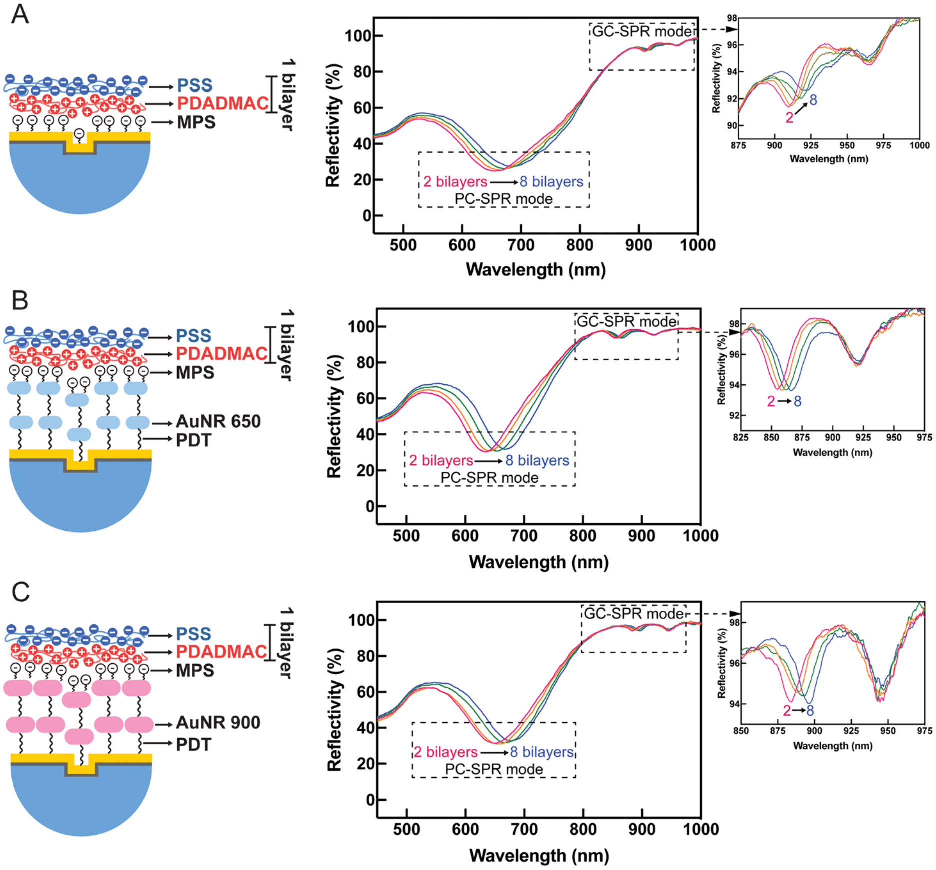

Fig. 8 SPR reflectivity curves of PDADMAC/PSS bilayers ranging from 2 to 8 bilayers (bls) under various experimental conditions: (A) without the addition of AuNRs, (B) with the addition of 650 layers of AuNRs, and (C) with the addition of 900 layers of AuNRs.

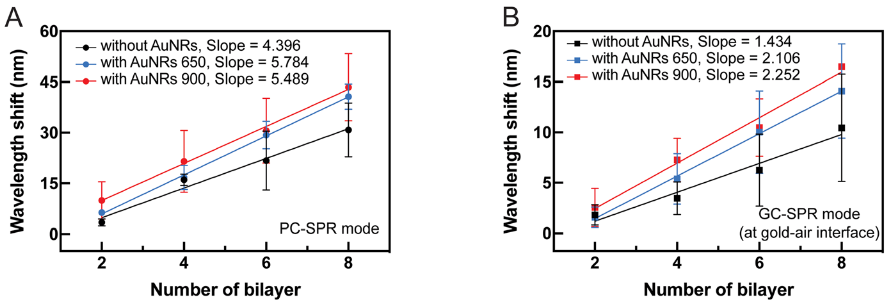

Fig. 9 Comparison of linear regression plots depicting the relationship between the number of PDADMAC/PSS bilayers and the wavelength shift in both (A) the PC-SPR mode and (B) the GC-SPR mode at the gold–air interface. Three distinct scenarios are represented in the plots: no AuNRs added (black dots), AuNRs 650 added (blue dots), and AuNRs 900 added (red dots).

cases without and with 2 layers of AuNRs 650. Specifically, the slope of the linear fitting in the GC-SPR mode increased by 1.57 compared to the absence of AuNRs and by 1.07 compared to adding two layers of AuNRs 650. The observed results confirm that the fabricated SPR sensor chip exhibited sensitivity to changes in the complex refractive index at the surface of the gold-coated grating prism. This sensitivity is evident in the augmented slope of the linear fitting, indicating the ability to detect and respond to changes in the refractive index of the surrounding medium. These findings emphasize the SPR sensor chip's sensitivity to variations in the complex refractive index at the surface of the gold-coated grating prism, as demonstrated by the increased slope of the linear fitting upon the addition of AuNRs 650 and 900. Moreover, the dual-mode SPR sensor chip demonstrated the capability to selectively detect specific SPR modes by utilizing materials with refractive indices corresponding to the wavelength of the targeted SPR excitation mode. Although we did not observe clearly the coupling between two types of propagating or extended surface plasmons, *i.e.*, PC-SPR and GC-SPR and localized surface plasmons, the enhanced sensitivity might be related to the coupling as seen in the broadened SPR dip shown in Fig. 8. Further improvement of the selectivity might be possible by controlling the alignment of the AuNRs and effectively utilizing longitudinal localized surface plasmons in order to obtain the strong coupling between propagating surface plasmons and localized surface plasmons.[34–36] This selective detection underscores the versatility and potential applications of the dual-SPR sensor chip in biosensing and related fields.

Conclusions

We have successfully utilized soft lithography and the confined sessile drop technique to fabricate a NOA 61 polymeric grating prism. This innovative prism fabrication allows the development of a dual-mode SPR sensor chip capable of exhibiting PC-SPR and GC-SPR excitation modes. Incorporating these two modes on a single sensor chip allows the simultaneous detection of SPR-sensitive shifts in visible and near-infrared (NIR) regions, representing a significant advancement in optical sensing technology. Examination of the imprinted grating pattern on the NOA 61 polymeric grating prism confirms successful fabrication, opening up possibilities for utilizing the NOA 61 polymeric prism in various optical and sensing devices. Furthermore, our study explored dynamic shifts in SPR excitation wavelengths by analyzing the dependence of reflectance on incident angle and refractive index. The refractive index sensitivity analysis confirmed that the PC-SPR mode was more responsive than the GC-SPR mode. Additionally, the dual-mode SPR sensor chip demonstrated successful detection of human IgG. Real-time responses from PC-SPR and GC-SPR modes at the gold layer/air interface showcased the biosensor's capability to detect anti-IgG attachment and subsequent IgG adsorption. Integrating AuNRs and PDADMAC/PSS bilayers in the dual-mode SPR sensor chip enhances sensitivity and selectivity. AuNRs with specific plasmon excitation wavelengths (650 and 900 nm) ensure tailored excitation for PC-SPR and GC-SPR modes, resulting in significant redshifts. The layer-by-layer assembly of PDADMAC/PSS bilayers further provides tunable properties, establishing a versatile platform for developing sensitive and selective SPR sensing. Consequently, the dual-mode SPR sensor chip holds great promise for driving scientific and technological progress in optical sensing.

Data availability

The data that support the findings of this study are available from the corresponding author upon reasonable request.

Author contributions

Wisansaya Jaikeandee: conceptualization, methodology, validation, investigation, data curation, writing – original draft & review & editing. Supeera Nootchanat: conceptualization, methodology, writing – review & editing. Chutiparn Lertvachirapaiboon: conceptualization, nethodology, writing – review & editing. Sanong Ekgasit: conceptualization, methodology, writing – review & editing. Kazunari Shinbo: conceptualization, methodology, writing – review & editing. Keizo Kato: conceptualization, methodology, writing – review & editing. Akira Baba: conceptualization, methodology, supervision, project administration, funding acquisition, writing – review & editing.

Conflicts of interest

There are no conflicts of interest to declare.

Acknowledgements

This work was supported by Japan Society for the Promotion of Science (JSPS) KAKENHI Grant Numbers JP20H02601 and JP24K01328.

References

1 J. Zhou, Q. Qi, C. Wang, Y. Qian, G. Liu, Y. Wang and L. Fu, *Biosens. Bioelectron.*, 2019, **142**, 111499.

2 Y. Huang, L. Zhang, H. Zhang, Y. Li, L. Liu, Y. Chen, X. Qiu and D. Yu, *Micromachines*, 2020, **11**, 526.

3 C. Y. Chain, M. A. Daza Millone, J. S. Cisneros, E. A. Ramirez and M. E. Vela, *Front. Chem.*, 2021, **8**, 605307.

4 M. Garrido-Jareño, L. Puchades-Carrasco, L. Orti-Pérez, J. M. Sahuquillo-Arce, M. del Carmen Meyer-García, J. Mollar-Maseres, C. Lloret-Sos, A. Gil-Brusola, J. L. López-Hontangas, J. M. Beltrán-Garrido, J. Pemán-García and A. Pineda-Lucena, *Sci. Rep.*, 2021, **11**, 6502.

5 M. Trzaskowski, A. Mazurkiewicz-Pisarek, J. W. Trzciński, M. Drozd, R. Podgórski, A. Zabost and E. Augustynowicz-Kopeć, *Sensors*, 2023, **23**, 3946.

6 P. Zhang, Y. P. Chen, W. Wang, Y. Shen and J. S. Guo, *TrAC, Trends Anal. Chem.*, 2016, **85**, 153.

7 J. Homola, *Chem. Rev.*, 2008, **108**, 462.

8 J. Homola, S. S. Yee and G. Gauglitz, *Sens. Actuators, B*, 1999, **54**, 3.

9 B. D. Gupta and R. Kant, *Opt. Laser Technol.*, 2018, **101**, 144.

10 S. S. Hinman, K. S. McKeating and Q. Cheng, *Anal. Chem.*, 2018, **90**, 19.

11 B. Turker, H. Guner, S. Ayas, O. O. Ekiz, H. Acar, M. O. Guler and A. Dâna, *Lab Chip*, 2011, **11**, 282.

12 J. Albert, S. Lepinay, C. Caucheteur and M. C. DeRosa, *Methods*, 2013, **63**, 239.

13 Y. Saito, Y. Yamamoto, T. Kan, T. Tsukagoshi, K. Noda and I. Shimoyama, *Opt. Express*, 2019, **27**, 17763.

14 W. Su, Y. Luo, Y. Ding and J. Wu, *Sens. Actuators, A*, 2021, **330**, 112858.

15 M. Wu, N. Xu, E. Wang, S. Gen, H. Zhu, C. Liu and J. Cao, *Appl. Surf. Sci.*, 2022, **603**, 154446.

16 E. Laffont, N. Crespo-Monteiro, A. Valour, P. Berini and Y. Jourlin, *Sensors*, 2023, **23**, s23031188.

17 C. J. Alleyne, A. G. Kirk, R. C. Mcphedran, N.-A. P. Nicorovici and D. Maystre, *Opt. Express*, 2007, **15**, 8163.

18 F. Bahrami, J. S. Aitchison and M. Mojahedi, *IEEE Photonics J.*, 2015, **7**, 48005607.

19 S. H. El-Gohary, S. Eom, S. Y. Lee and K. M. Byun, *Opt. Commun.*, 2016, **370**, 299.

20 P. Arora, E. Talker, N. Mazurski and U. Levy, *Sci. Rep.*, 2018, **8**, 9060.

21 H. Guo, P. Zhang, S. Wang, Y. Pan, X. Wang, Z. Wang and Y. Gong, *Plasmonics*, 2021, **16**, 2249.

22 C. Lertvachirapaiboon, A. Baba, K. Shinbo and K. Kato, *Anal. Chim. Acta*, 2021, **1147**, 23.

23 D. S. Wang and S. K. Fan, *Sensors*, 2016, **16**, 1175.

24 C. Xiao, J. Eriksson, A. Suska, D. Filippini and W. C. Mak, *Anal. Chim. Acta*, 2022, **1201**, 339606.

25 S. Nootchanat, W. Jaikeandee, P. Yaiwong, C. Lertvachirapaiboon, K. Shinbo, K. Kato, S. Ekgasit and A. Baba, *ACS Appl. Mater. Interfaces*, 2019, **11**, 11954.

26 Norland Products Inc., Norland Optical Adhesive 61, **https://www.norlandprod.com/adhesives/NOA%2061.html** (accessed October 1 2021).

27 J. R. Wimperis and S. F. Johnston, *Appl. Opt.*, 1984, **23**, 1145.

28 S. Ekgasit, N. Kaewmanee, P. Jangtawee, C. Thammacharoen and M. Donphoongpri, *ACS Appl. Mater. Interfaces*, 2016, **8**, 20474–20482.

29 B. A. Prabowo, A. Purwidyantri and K. C. Liu, *Biosensors*, 2018, **8**, 80.

30 J. Cao, Y. Sun, Y. Kong and W. Qian, *Sensors*, 2019, **19**, 405.

31 J. Homola, in *Surface plasmon resonance (SPR) sensors*, ed. J. Homola and Springer, Springer-Verlag Berlin Heidelberg, 2006, p. 3.

32 A. Baba, K. Kanda, T. Ohno, Y. Ohdaira, K. Shinbo, K. Kato and F. Kaneko, *Jpn. J. Appl. Phys.*, 2010, **49**, 01AE02.

33 E. T. Fogg, A. N. Hixson and A. R. Thompson, *Anal. Chem.*, 1955, **27**, 1609.

34 M. Abutoama, S. Li and I. Abdulhalim, *J. Phys. Chem. C*, 2017, **121**, 27612–27623.

35 S. K. Srivastava, A. Li, S. Li and I. Abdulhalim, *J. Phys. Chem. C*, 2016, **120**, 28735–28742.

36 T. Thepudom, C. Lertvachirapaiboon, K. Shinbo, K. Kato, F. Kaneko, T. Kerdcharoen and A. Baba, *MRS Commun.*, 2018, **6**, 107–112.